

CFD Analysis of Solar Tower Hybrid Pressurized Air Receiver (HPAR) using a Dual-Banded Radiation Model

K.J. Craig^{a,*}, P. Gauché^b and H. Kretzschmar^c

^aProfessor, PhD, solarUP, Thermoflow Research Group, Department of Mechanical and Aeronautical Engineering,
University of Pretoria, Pretoria 0002 South Africa

^bSenior researcher and director, M.Sc Eng, °M.Sc Eng graduate, Solar Thermal Energy Research Group, Stellenbosch
University, Private Bag XI Matieland 7602 Stellenbosch South Africa

* Corresponding author: ken.craig@up.ac.za +27-12-420-3515

Abstract

Solar receivers used for central tower Concentrated Solar Power (CSP) plants use either a surface-based or volumetric heat transfer region. Volumetric receivers are more efficient but require more sophisticated and expensive materials that can withstand the elevated temperatures (in excess of 1000°C). For a solarized gas-turbine application, pressurized air from the compressor is used as heat transfer fluid (HTF) in order to increase both the density and heat capacity of the HTF. If a volumetric receiver is used, it needs to be located in a pressure vessel with a pressurized quartz window located at the aperture of the concentrator. An alternative approach to utilize pressurized air in a pseudo-volumetric fashion is to populate a volumetric region with piped pressurized air. A tubular-type volumetric receiver (named a Hybrid Pressurized Air Receiver (HPAR)) is studied here. The HPAR provides the challenge of enabling maximum heat transfer without causing hot spots on the side of the solar irradiation source. Heat transfer in the HPAR would not be as effective as for a true volumetric receiver because the heat transfer area is limited by the tube wall. The heat transfer to the HTF is however enhanced through mixing generated by external forced convection caused by suction due to a downstream fan in the receiver cavity. In addition, the aperture of the cavity contains a glass windowed louver system, to limit re-radiation losses. A Computational Fluid Dynamics (CFD) model is generated of the solar receiver cavity. The commercial CFD code ANSYS Fluent v14.5 is used to evaluate the heat transfer between the incoming solar flux and the HTF. A numerical validation is performed to illustrate mesh dependency and the choice of turbulence model. The incoming solar irradiation and its absorption, reflection and transmission are modeled using the Discrete Ordinates (DO) radiation model in ANSYS Fluent. An idealized and a solar flux map based on the PS10 field are used as source. For comparison, both a gray (without a glass louver) and a semi-gray two-banded DO approach are used when modeling the absorption of high-wavelength re-radiation by the glass in front of the aperture. This two-banded approach is also applied to investigate the influence of a band-selective absorber tube and cavity surfaces. The DO model also predicts the emission of thermal re-radiation from all surfaces. The geometry is parameterized in order to allow for various cavity layouts to be automatically generated. Results include typical CFD results of a candidate geometry to illustrate the solar irradiation input, the effect of tubular layout as well as temperature and heat flux

distributions for single and dual-band radiation.

Keywords: Cavity receiver; CFD; Hybrid pressurized air receiver; radiation modeling

1. Introduction

Tubular receivers are compared to ideal volumetric receivers in Fig. 1. Because of the porosity and large extinction volume of volumetric receivers, the solar irradiation penetrates deeper into the receiver causing a gradual temperature rise of the solid material (Ávila-Marín, 2011). The leading face of the tubular receiver, on the other hand, heats up to the highest temperature because of the high resistance to heat transfer of the tube material. Generally, tube receivers lack thermal efficiency and high receiver outlet temperatures. This is associated with the thermal conductivity of the tubes which restricts effective heat transfer to the heat transfer fluid (HTF). Also, material constraints of the receiver tubes due to high thermal stresses and non-uniform flux distribution around the tubes cause leakages and hot-spots are generated (Kretzschmar & Gauché, 2012, Kretzschmar, 2014).

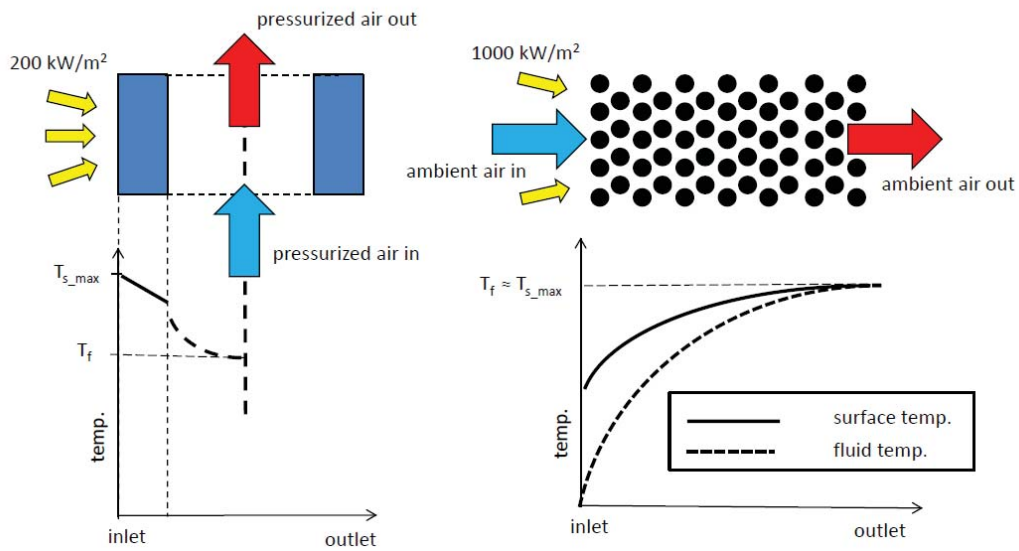


Fig. 1. Comparison of temperature distribution in tubular and volumetric receivers.

Requirements for a volumetric receiver are the resistance to temperature as high as 1000°C, high porosity for a sufficiently large extinction volume such that the concentrated solar radiation

penetrates through the receiver, high cell density to achieve large specific surface area and sufficiently high effective thermal conductivity to avoid possible thermal spots (Sano et al., 2012). The ideal temperature rise for volumetric receivers is somewhat compromised in the numerical modeling of porous receiver materials like those considered by Sano et al. (2012) and Smirnova et al (2010). Sano et al. (2012) show how the solid material does experience the highest temperature at the inlet face before decreasing slightly.

For pressurized air as working fluid (as found in solarized gas turbines), a porous volumetric receiver would require a pressurized quartz window to enable the whole receiver to operate under high pressure, as opposed to open volumetric receivers that use ambient air (Hoffschmidt et al., 2003). In an attempt to combine the benefits of the volumetric receiver as well as negate the need for a quartz window, the Hybrid Pressurized Air Receiver (HPAR) concept was proposed by Kretzschmar & Gauché (2012). HPAR consists of three zones, the secondary concentrator, the cavity and the secondary heat exchanger (which is a counter-flow heat exchanger) (Kretzschmar, 2014). The secondary concentrator, called compound parabolic concentrator (CPC), is optional to the design as it depends on the concentration factor achieved by the heliostat field. The receiver's thermodynamic cycle can be separated into two different loops, i.e., a pressurized air loop, and an unpressurized air loop. Before entering the receiver cavity, the pressurized air loop is routed such that it is preheated by the unpressurized air loop. In the cavity, the pressurized air is further heated by irradiated tube bundles to the final maximum outlet temperature. The unpressurized air loop is similar to the open volumetric receiver concept where ambient air is being sucked into the receiver and is heated up by the absorber material. The enthalpy gained by the volumetric air stream that is not used during the preheating described above, is either recovered by means of a secondary heat exchanger or routed to a storage system like a packed rock bed (Allen et al., 2013).

The cavity aperture is covered by a transparent window (i.e., louvers or glass panes/tubes) such that while it transmits most of the solar irradiation associated with the solar spectrum, it is opaque to most of the wavelengths associated with emitted re-radiation from the array of absorber tubes inside the cavity due to their temperature. The effect of modeling the glass is evaluated by including it in the model or omitting it. The switch for opaqueness is implemented using a dual-banded approach for the absorption coefficient value.

To investigate a band-selective absorber, the dual-banded approach is also used to limit the re-radiation of the absorber tubes by giving them a lower emissivity at high infrared wavelengths as opposed to a high emissivity (= high absorptivity) at low wavelengths.

The current paper is focused on the cavity of the HPAR and assesses the combination of heat penetration, re-radiation and external forced convection using Computational Fluid Dynamics (CFD). In order to model the correct heat input from solar irradiation, a test case was constructed to

investigate how to represent solar flux from a heliostat field. The paper then describes how the cavity geometry was parameterized in order to automatically generate different representations of the HPAR concept. A numerical validation study of forced convection over a tube bank is presented to illustrate mesh dependency and turbulence model selection. A base geometry, that compares the effect of modeling the wavelength band-dependent absorption characteristics of glass versus omitting the glass, is evaluated to illustrate the performance through detail and integrated CFD results. In the evaluation of the base geometry, the ideal heat source used in the solar irradiation test case is also compared to a solar heat flux map obtained from a SolTrace simulation of the PS10 heliostat field (Marsberg et al., 2014).

2. Solar irradiation

The Discrete Ordinates (DO) thermal radiation model in ANSYS Fluent (ANSYS, 2012) can be used to model a solar irradiation source field by defining semi-transparent walls at the boundary of the computational domain. Each 'source' wall can be modeled as semi-transparent to mimic a mirror reflecting solar irradiation at a specific specular angle. By dividing a plane into many subsections, and assigning an irradiation direction to each that is pointed towards a specific target, the concentration effect of a heliostat onto a central receiver can be approximated. Fig. 2 shows a test case geometry where a 12x12 array of square 0.125x0.125m sources point towards a target plane. The target is given an emissivity of 1 to allow it to absorb all incoming irradiation as dictated by Kirchhoff's law. Each source is given a direct irradiation flux value of 1.667MW/m^2 , a beam angle of 0.53° and a direction vector aimed at the center of the target. The source radiation flux distribution and target absorbed radiation flux are shown in Fig. 3. Note that the effective source values of the outlying sources are less due to the projection of the specified value onto the source direction, i.e., the constant source value is multiplied by the cosine of the angle between ray direction and the surface normal. The concentration effect on the target can clearly be seen. An extension of this test case included a simplified cavity receiver with three tubes. The emissivity on the tube walls was set at 0.9 so that they each absorb 90% of the incoming radiation as well as that reflected off other surfaces, while the cavity walls have an emissivity/absorptivity of 0.1 to set their reflectivity at 90% (the default setting in ANSYS Fluent was used in this work, i.e., a gray assumption where emissivity equals absorptivity according to Kirchhoff's law across the whole wavelength spectrum). For this solar absorption-only study, the specified surface emissivity translates to a solar absorptance only, and the value of 0.9 is typical of good solar absorbers (Modest, 2013) as a gray value representative of the solar spectrum for all absorber temperatures. The cavity and tube surfaces are all opaque and gray and reflect diffusely. Their temperature was

set at 10K to limit the emission component of radiation, i.e., the surfaces mostly act as absorbers or reflectors, not emitters. The radiation flux at the cavity entrance is displayed in Fig. 4 together with the absorbed and reflected radiation in the cavity. The highest absorption occurs at the center of the tubes because of the shadowing effect of the cavity walls.

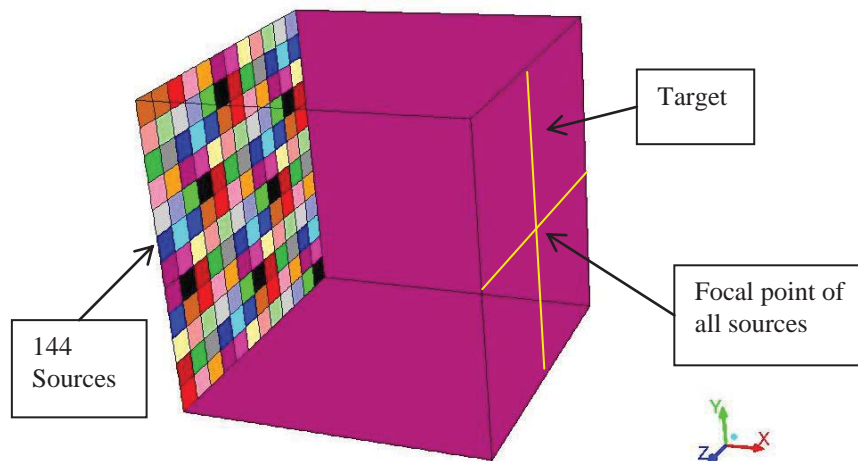
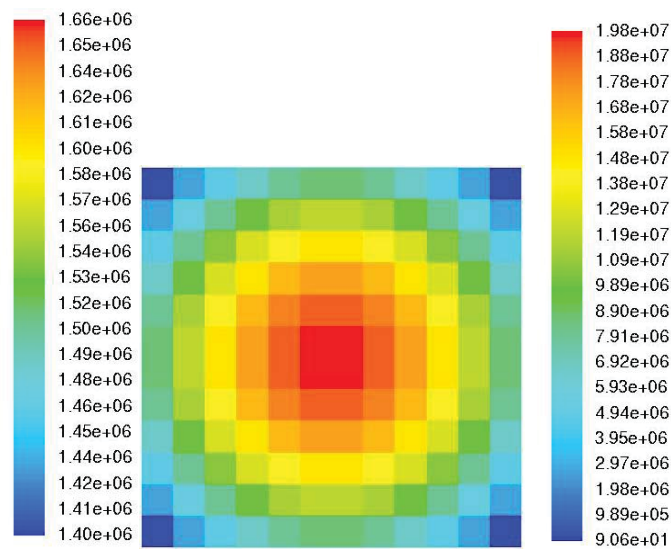


Fig. 2. Geometry of test case for solar irradiation.



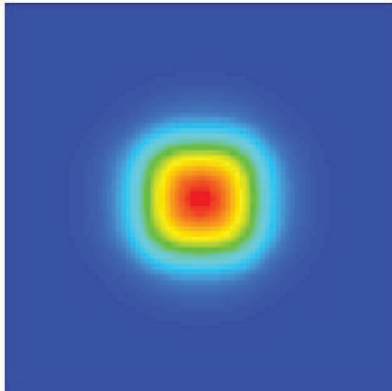
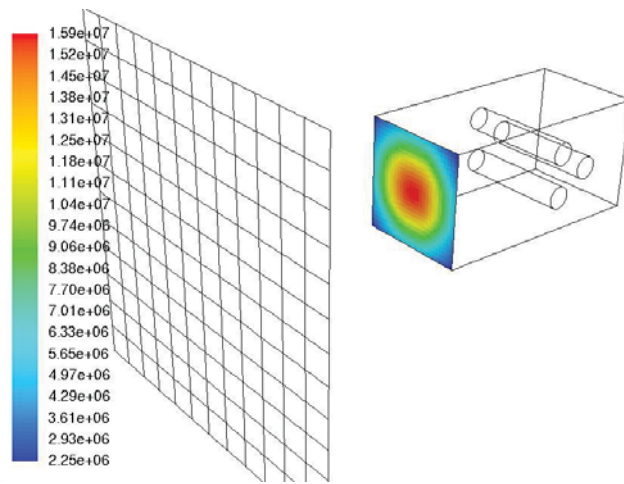
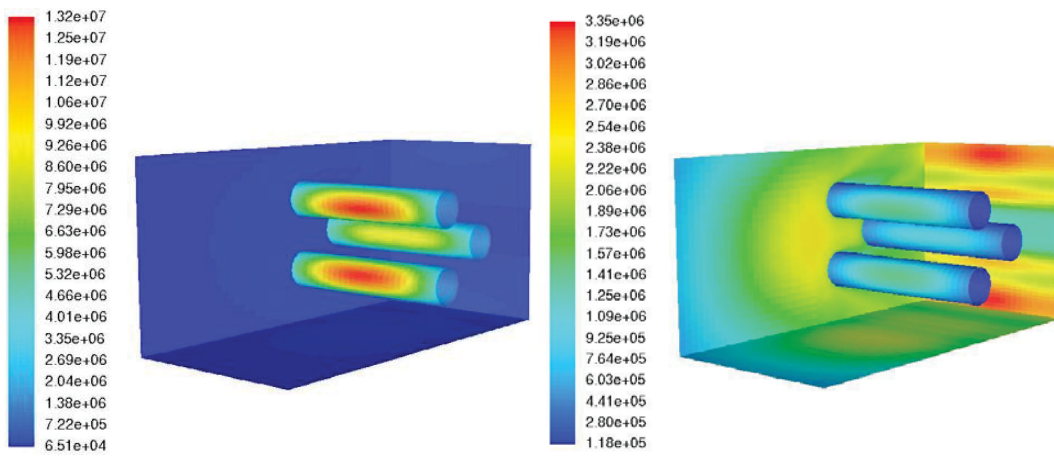


Fig. 3. Effective source flux distribution (left); Absorbed radiation flux on target (right) [W/m²]. Single gray band.



a)



b)

c)

Fig. 4. a) Radiation flux at cavity aperture; b) Absorbed radiation flux on cavity surfaces; c) Reflected radiation flux on cavity surfaces [W/m^2]. Single gray band.

3. Parameterization of geometry

The parameterization capability of the geometry and mesh generator, GAMBIT, was extensively utilized in the definition of the receiver geometry. A master journal file was generated that calls other journal files and executes system commands which generate additional journal files that depend on parameter settings. In this way, the layout of the cavity, tubular arrangement, tube size, header and piping layout associated with the HTF loop, etc., can be automatically generated based on a set of defining input parameters.

A symmetric geometry in the vertical direction was considered. The structure of the geometry and mesh generation process is summarized in Fig. 5. In order to allow for a tubular layout of varying porosity (to allow solar irradiation to penetrate deeper into the cavity), an elliptical region was defined where tubes are spaced based on two defining dimensions (base pitch and front-facing pitch) as indicated in Fig.6. The use of a variable porosity (elliptical) region to allow deeper penetration of radiation is modeled after the radiation characteristics of porous media thermal insulation. Increasing the porosity decreases the optical thickness and the extinction coefficient. The sizes of the tubes and tube spacing are orders of magnitude larger than the wavelengths of the incoming solar irradiation and hence the porosity would not have a spectral affect. The view factor effects (both for reflection and emitted re-radiation) are therefore dominant in allowing further penetration. The rest of the cavity is populated using a regular triangular arrangement. Sample tube layouts generated in this fashion are shown in Fig. 6. To distribute the HTF through the cavity, a header system is used. Because of the *à priori* unknown location of tubes in the variable porosity region, logic is used to project a specific tube onto the nearest header (Fig. 7). In this way vertical banks of tubes are connected to a common header. The number of and size of the headers are dependent on the tube size, tube number and cavity size (see samples in Fig. 6). The routing between headers was implemented in a particular fashion so as to let the front-facing tubes have the coldest HTF which then snakes through the domain. The forced convection in the cavity exterior to the tubes containing the HTF is enabled through slots in louvers on the left-hand faces in Fig. 6. The outlet of the cavity is in the form of multiple thin slots on the right-hand faces in Fig. 6. Both inlet and outlet configurations are also parameterized. The configuration in Fig. 7b) is used as base geometric case in this paper.

For the case of a glass cover, a 10mm-thick solid glass volume is modeled (see Fig. 8). The inlets to the cavity are still modeled in the same way, i.e., as slots from which the air emanates into the cavity domain. This boundary condition is applied by specifying an inlet face *and* a wall coincidentally at the same location. The inlet is adjacent to the cavity fluid domain, while the wall is adjacent to a domain modeled as a solid with the properties of air, i.e., being reasonably insulating, but transparent to radiation. This arrangement mimics a louver system (see explanatory insert in Fig. 8)

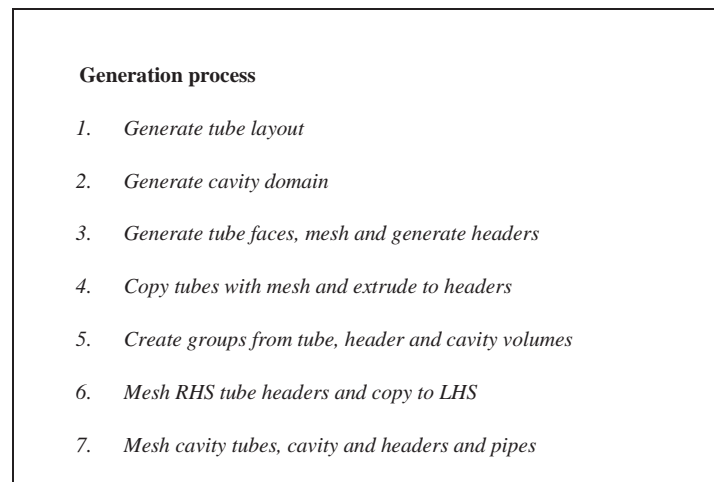


Fig. 5. Geometry and mesh generation process using journals and parameters in GAMBIT

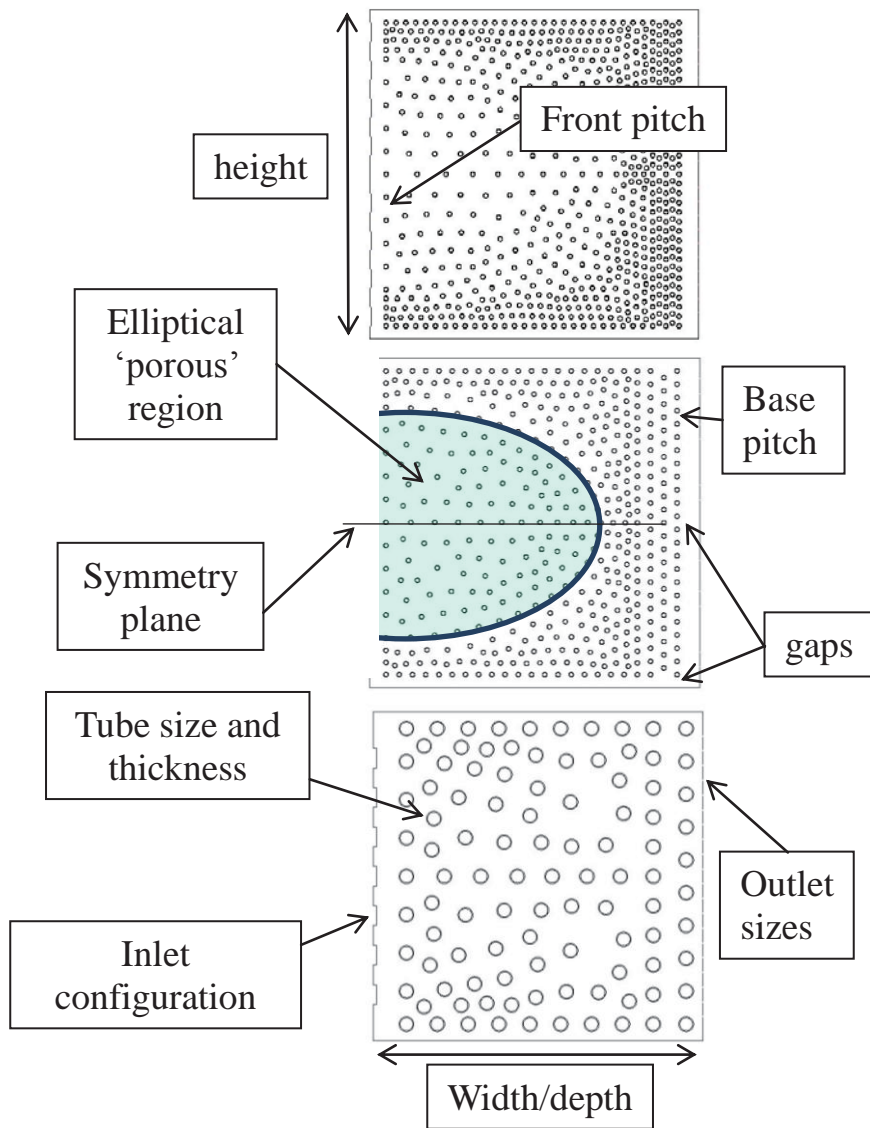


Fig. 6. Sample tubular layouts for different tube size and porosity parameters.

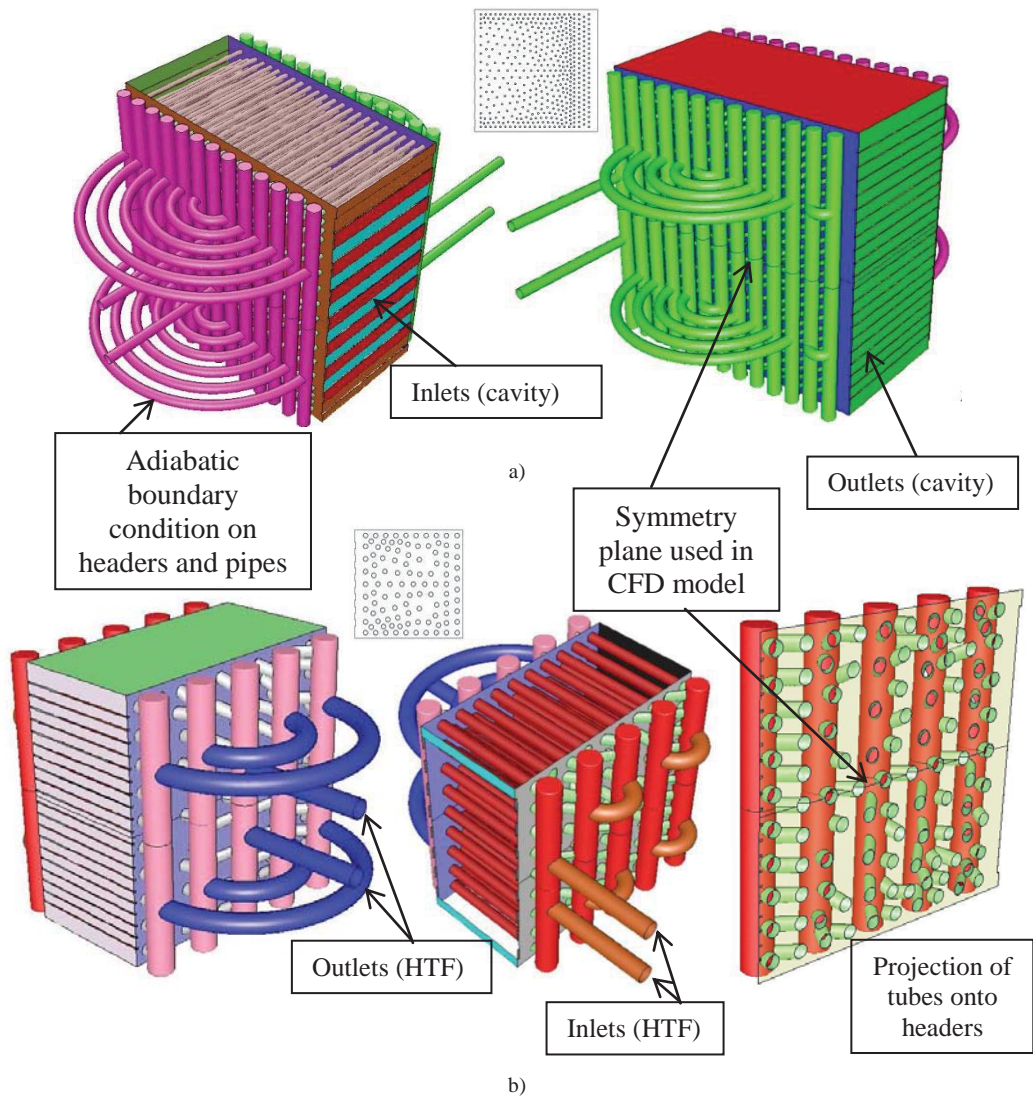


Fig. 7. Sample header configurations a) Many, small tubes; b) Fewer, larger tubes, also showing tube projection onto closest header. Inserts showing tubular layout.

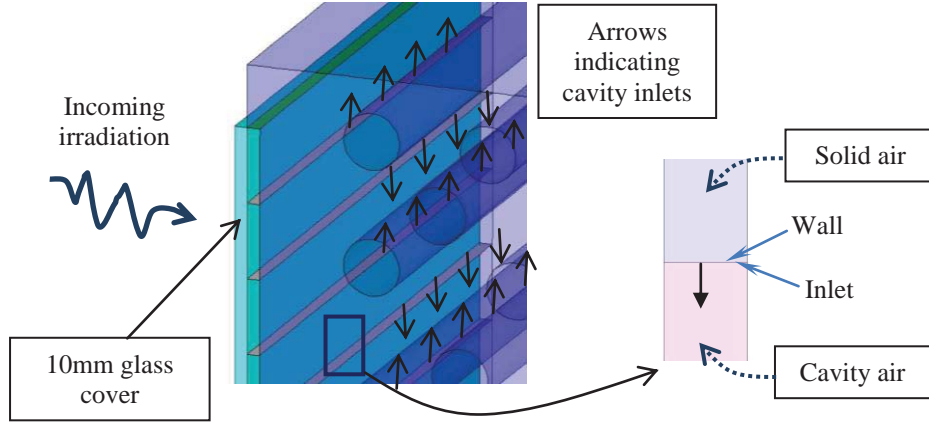


Fig. 8. Geometric detail of glass cover and location of inlets into cavity. Insert showing implementation of inlet boundary condition.

4. CFD model settings, boundary conditions and properties

4.1. Cell zone settings

In order to combine the solar irradiation heat source with the cavity and HTF loop, certain modeling assumptions are made as in Craig et al. (2013), with the exception that a single radiation band was considered in that study. The air external to the receiver through which the solar flux is transmitted, is modeled as a solid zone that participates in radiation, but with zero absorptivity and the refractive index of air (vacuum). Because of this assumption, the fluid flow and turbulence model equations are not solved in this zone, reducing the computational time of the model. The pressurized air inside the HTF loop is set to not participate in thermal radiation to reduce the zones where the expensive DO equations are solved. As the internal surfaces of the tubes and header pipes are locally at similar temperatures, this is a good assumption. This assumption implies that the heat transfer mechanisms inside the tubes are conduction and convection only, i.e., the heat source is conducted through the tube walls and then transferred to the HTF through convection. When included in the model, the glass of the aperture window is given a refractive index of 1.5, a value representative of the wavelength band considered.

The absorption coefficient of a semi-transparent participating medium relative to its absorption (Modest, 2013) is defined in equation (1):

$$\alpha_{\eta} = 1 - \tau_{\eta} = 1 - e^{-\kappa_{\eta}s} \quad (1)$$

where α_{η} and τ_{η} are the absorptivity and transmissivity at a specific wavenumber, respectively, s the thickness of the medium and κ_{η} the absorption coefficient. In the two bands (smaller and larger than $4.25\mu\text{m}$, respectively), values of the absorption coefficient of 106 and 2300m^{-1} , respectively,

are used. For a 10mm-thick glass window, these correspond to absorptivity values of 0.65 and approximately 1, respectively. The latter means that radiation emitted at wavelengths above $4.25\mu\text{m}$ is mostly absorbed by the glass in the so-called greenhouse effect. Temperature sensitivity of the absorption coefficient values was assumed to be small and was therefore neglected.

4.2. Material properties

The fluid (air) external to the tubes inside the cavity is given separate properties from the HTF inside the tubes and headers. As the HTF pressure remains fairly constant, an incompressible assumption is made for density inside the tubes and headers. Due to the large fluid temperature variation in the cavity external to the tubes, the incompressible ideal gas assumption is made, where the density is a function of temperature only. For both these fluids, the thermal conductivity is specified as a piece-wise function of temperature in the respective ranges. The viscosity is described by Sutherland's law.

4.3. Turbulence modeling

Both the realizable $k\text{-}\epsilon$ and the SST $k\text{-}\omega$ turbulence model (ANSYS, 2012) are used to model turbulent flow in both the HTF loop and the external forced convection in the cavity. Refer to the numerical validation section in the Results for the evaluation of these models. Values for y^+ were below 200 for surfaces exposed to fluid flow (both in cavity and in HTF loop).

4.4. Surface properties and boundary conditions

The header pipes and tubes external to the cavity are assumed to be perfectly insulated, i.e., an adiabatic wall assumption is made for these external surfaces. All walls adjacent to a fluid are assumed to be smooth and no-slip. The absorber tubes in the cavity were given an emissivity of 1, implying that they emit perfectly as well as absorb perfectly (i.e., no incoming radiation is reflected). This selection represents a worst-case in that the hot spots (maximum temperature) would be accentuated and the re-radiation losses would be maximized. The emission is prescribed to be diffuse. For the dual-band implementation, a band-selective approach was followed for the semi-gray emissivity of the absorber tubes. While the emissivity in the lower band (where the solar irradiation is concentrated) is set to 1 (implying a solar absorptance of 1), the emissivity in the upper band is set to 0.1, implying that the temperature-dependent emission is only 10% of the Planck's law blackbody value. The latter is implemented in the solution Radiative Transfer Equation (RTE) and RTE boundary conditions as contained in the DO model of ANSYS Fluent.

For the dual-band approach for the glass window, the solar irradiation source is only applied in the low wavelength band, mimicking the transparency of the glass window in this part of the spectrum. The above is an attempt to model an ideal absorber, i.e., one that has a very high total solar absorptance, but a low hemispherical emittance at lower surface temperatures.

For the cavity walls, the single (gray) band value for emissivity (=absorptivity) prescribed was 0.1, while the dual band values were 0.1 for the lower band (containing the solar flux) and 0.9 for the upper band. For the case where a glass cover is modeled, the glass surfaces facing the cavity and the irradiation source are specified to be semi-transparent and to transmit radiation specularly.

As an initial case, the cavity cooling mass flow rate was set to 0.0125kg/s at an incoming ambient temperature of 27°C. The HTF was supplied at 500°C with a mass flow rate of 0.15kg/s.

4.5. Mesh

A relatively fine mesh was generated that has about 8.5 million cells. Sections of the mesh are shown in Fig. 9. As part of the numerical validation presented in the Results section 5.1, a mesh dependency study is included that evaluates the prediction of the pressure distribution for a tube in cross-flow and the prediction of convective heat transfer for an isolated tube in cross flow. Mesh adaption was also applied to the HPAR test case with a glass window to illustrate mesh dependency (see section 6.).

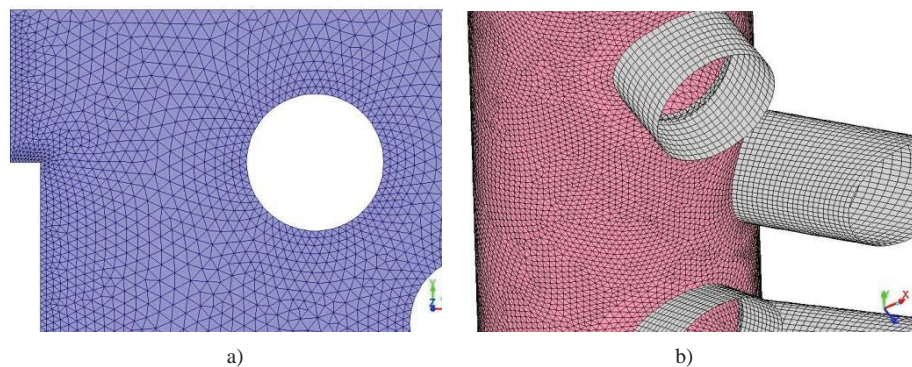


Fig. 9. Mesh on a) cavity wall, and b) header pipe and tube.

5. CFD results

5.1. Validation of numerical model

Case 1: Validation of pressure distribution around tube in tube bank

The test case (Case 86, Ercoftac (2014)) as described in Mahon & Meskell (2009) was repeated (see Fig. 10 for the 2-D symmetric computational domain with boundary conditions) to evaluate the ability of the turbulence models under investigation to predict the pressure distribution around a cylindrical tube in a staggered tube bank in the presence of cross-flow. A pitch ratio of 1.32 ($P = 50\text{mm}$, $d = 38\text{mm}$) was used. Three different tetrahedral (triangular) mesh sizes were considered as well as the built-in solution-adaptive re-meshing in ANSYS Fluent as a final mesh refinement step. A uniform velocity inlet corresponding to the Reynolds number of the experiment was applied at the inlet.

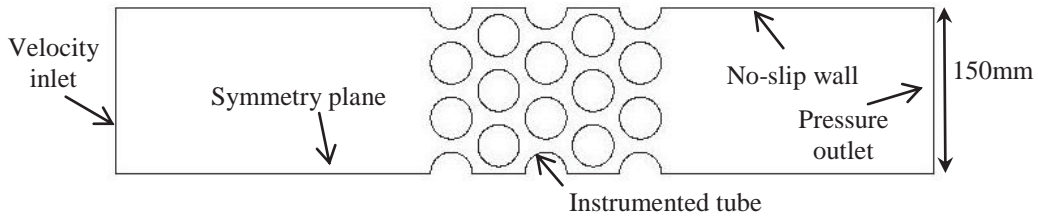


Fig. 10. Computational domain showing boundary conditions and instrumented tube (after Mahon & Meskell (2009)).

Both the SST $k-\omega$ and the realizable $k-\varepsilon$ (rke) turbulence model, the latter with enhanced wall treatment (EWT), were tested. The results are summarized in Figs. 11 and 12 with a representative flow pattern depicted in Fig. 13. The pressure coefficient is defined as in Mahon & Meskell (2009), as

$$C_p = 1 - \frac{P_{\theta_{\max}} - P_{\theta}}{\frac{1}{2} \rho U_g^2} \quad (2)$$

using the maximum circumferential pressure $P_{\theta_{\max}}$ as reference, with the gap velocity calculated based on an incompressible flow assumption, defined as

$$U_g = U \left[\frac{P}{P-d} \right] \quad (3)$$

When comparing the figures, the following observations can be made:

- The SST $k-\omega$ turbulence model over-predicts the pressure recovery behind the cylindrical tube, especially for coarse meshes.
- Refining the mesh allows the SST $k-\omega$ model to match the experimental data in the region of the stagnation point and at the maximum velocity location at $\theta = 90^\circ$.

- The realizable $k-\varepsilon$ model with EWT predicts the pressure minimum at $\theta = 90^\circ$ even with a coarse mesh. The pressure in the separated zone behind the tube is better predicted than with the SST $k-\omega$ model.
- When refining the mesh, the realizable $k-\varepsilon$ model however over-predicts the suction peak while matching the upstream and downstream distributions.

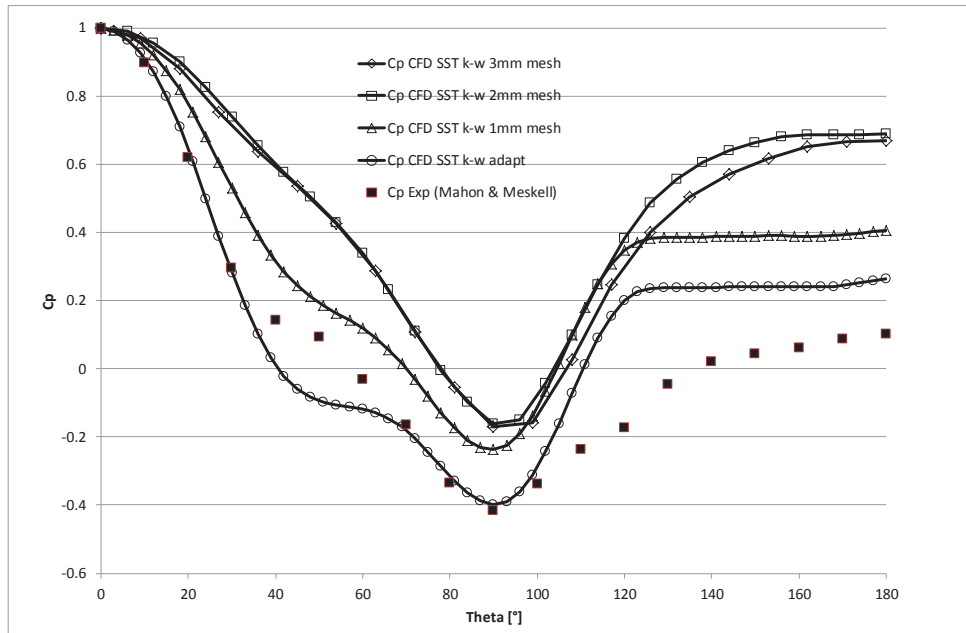


Fig.11. Pressure coefficient distribution comparison for CFD data using SST $k-\omega$ turbulence model and different mesh sizes with experimental data of Mahon & Meskell (2009).

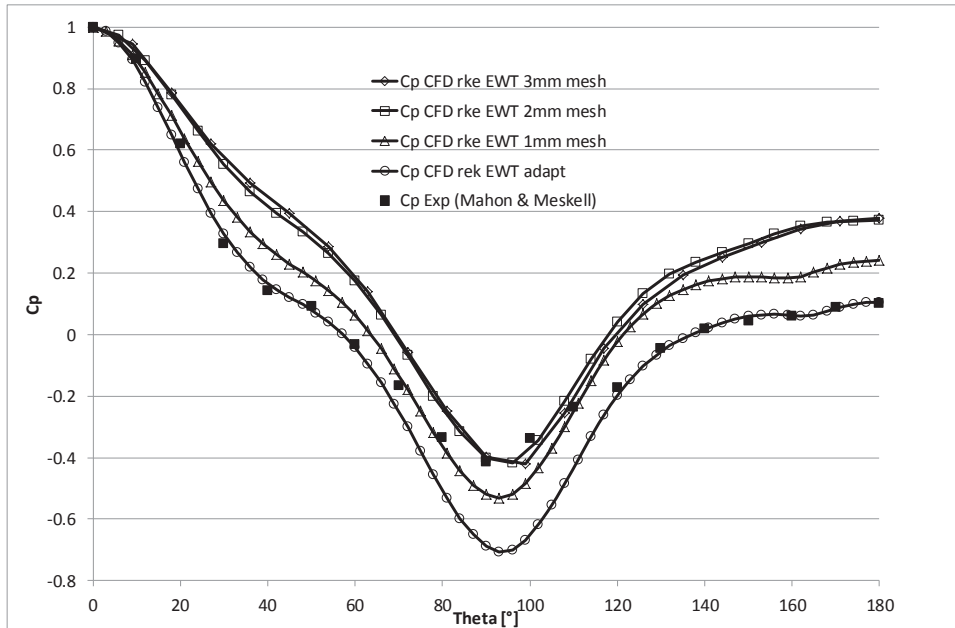


Fig.12. Pressure coefficient distribution comparison for CFD data using realizable $k-\epsilon$ turbulence model with Enhanced Wall Treatment (EWT) and different mesh sizes with experimental data of Mahon & Meskell (2009).

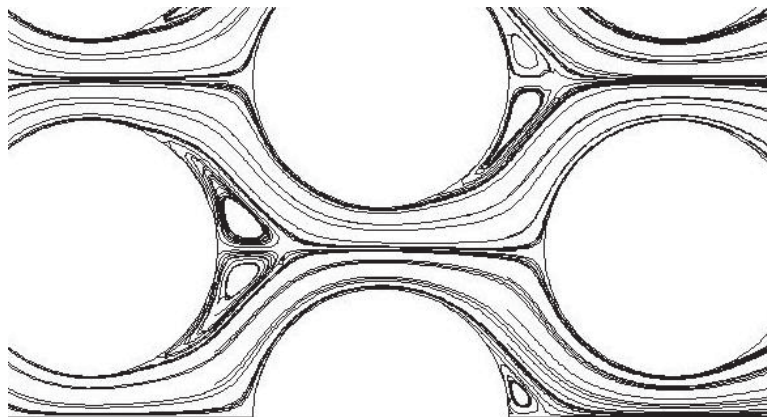


Fig.13. Streamlines around instrumented tube (realizable $k-\epsilon$ turbulence model with EWT).

Case 2: Validation of heat transfer around an isolated heat tube in forced convection

Following Hachicha (2013), the experiments of Scholten & Murray (1998a, 1998b) are used to validate the ability of the CFD code to predict the Nusselt number profile around an isolated heated tube. A 25mm-diameter tube was placed in a 127mm×127mm test section and heated with an internal cartridge heater. The convection heat transfer is estimated based on the electrically-dissipated heat as well as that conducted and used to calculate the local Nusselt number distribution:

$$Nu = \frac{q_{conv} D}{k_{air} (T_{sensor} - T_{ambient})} \quad (4)$$

In the CFD model (of which the boundary conditions are indicated on the computational domain in Fig. 14), a surface heat flux boundary condition corresponding to q_{conv} is used on the surface of the tube. This heat can only flow through convection into the computational domain. The local surface temperature (corresponding to the experimental T_{sensor}) is then used to calculate the Nusselt number according to equation (4). The inlet velocity is determined from the respective Reynolds number (Re) used in the experiment. No symmetry is used to allow for asymmetric flow to develop.

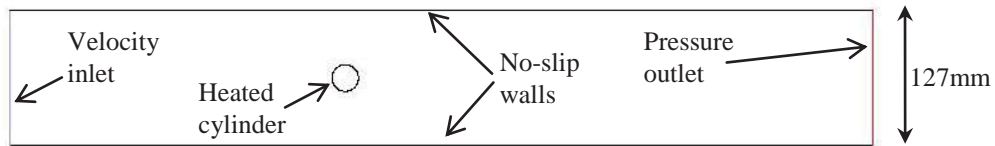


Fig. 14. Computational domain for isolated heat cylinder in 127×127mm duct.

The Nusselt number distribution around the top half of the cylinder is displayed in Fig. 15 for $Re = 7190$ for different mesh densities and compared to the high inlet turbulence experimental result from Scholten & Murray (1998b). Both the detail and average Nusselt numbers are shown. The realizable k- ϵ turbulence model is used for this comparison. The average Nusselt numbers are listed in Tab. 1 with the maximum y^+ value obtained in each simulation corresponding to the meshes of which close-ups are displayed in Fig. 16. At this Reynolds number, the boundary layer on the cylinder is still laminar although there are fluctuations in heat transfer due to the upstream turbulence as evidenced by the RMS error bars in Fig. 15 (obtained from Scholten & Murray (1998b)). As the mesh is refined, the respective CFD result comes closer to the experimental distribution, but the assumption of full isotropic turbulence in the realizable k- ϵ turbulence model means that it is unable to capture the peak Nusselt number at the stagnation point, regardless of mesh density. The separation location is over-predicted by the coarser meshes but the heat transfer in the wake is fairly well predicted and independent of the mesh density. The triangular and quadrilateral meshes of similar density produce similar distribution results with the stagnation-point Nusselt number being under-predicted. For the average Nusselt number around the cylinder, the triangular mesh provides a prediction within 15% while the quadrilateral mesh somewhat fortuitously predicts an average within 7% due to an improved minimum Nusselt number at separation. The addition of a boundary-layer mesh improves the prediction of the peak Nusselt

number at the stagnation point, but the heat transfer is over-predicted before the separation point. Using a boundary layer with a very fine mesh activates the enhanced wall treatment (EWT) option as the maximum y^+ value is below 11. Tab. 1 also lists the average Nusselt number obtained when using the SST $k-\omega$ turbulence model for the finest mesh which matches the experiment to within 1%. This detail result is discussed in the next section.

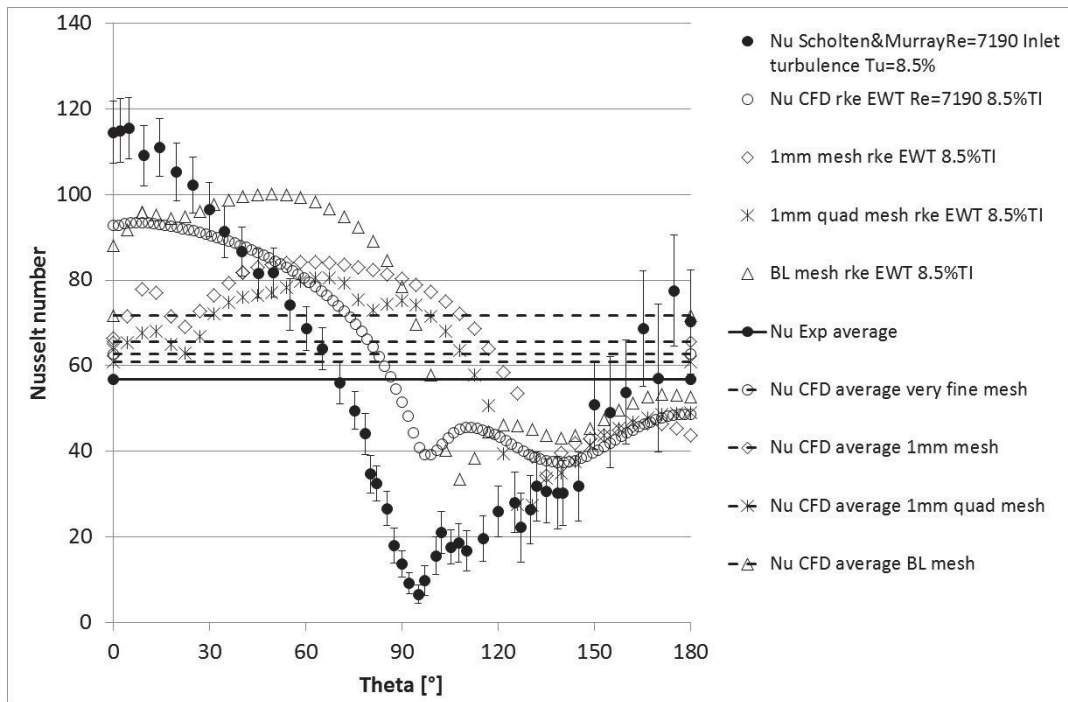


Fig.15. Nusselt number distribution around cylinder: high inlet turbulence experiment versus realizable $k-\epsilon$ turbulence model for different mesh densities and mesh types – $Re = 7190$.

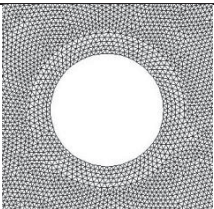
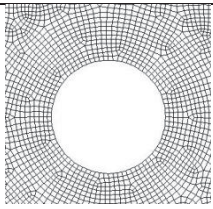
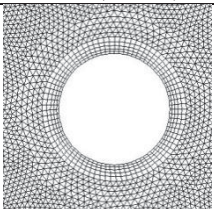
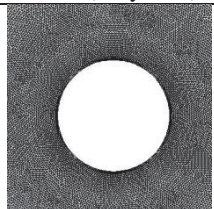
Mesh	1mm tetrahedral mesh	1mm quadrilateral mesh	Boundary layer mesh (coarse)	Boundary layer mesh (very fine)
Close-up				

Fig.16. Mesh types used for validation for $Re = 7190$.

Tab. 1. Summary data for mesh dependency comparison: $Re = 7190$.

Mesh	Average Nu	% deviation from experiment	Maximum y^+ on cylinder
------	------------	-----------------------------	---------------------------

Experiment	56.9	-	-
1mm tetrahedral mesh	65.6	15.3	14.3
1mm quadrilateral mesh	60.9	7.1	23.7
Boundary layer mesh (coarse)	71.8	26.2	14.3
Boundary layer mesh (very fine) (realizable k- ϵ /SST k- ω turbulence model)	62.7/56.5	10.1/0.788	2.6/2.6

Because of the fact that the velocity distribution in the HPAR cavity varies because of tube layout and as a function of cavity forced convection flow rate, the prediction of heat transfer is repeated for several Reynolds numbers. For the initial external convection mass flow rate considered in the HPAR simulation, most regions of the cavity flow around the HTF pipes experience laminar flow, except those near the slots or gaps between the tubes and the cavity walls.

The Nusselt number distributions around the top half of the cylinder is displayed in Figs. 17 through 19 for $Re = 7190, 21580$ and 43140 , respectively, with the very fine mesh (Fig. 16) being used. This Reynolds number range represents from laminar to turbulent cylinder boundary layers on the tube surfaces. The experimental values used for comparison are the high inlet turbulence values from Scholten & Murray (1998b). Using these results for comparison is motivated by the fact that most of the tubes in the proposed HPAR cavity are either in the wake of another tube, or receive their oncoming flow from jets meaning from slots between the glass window sections at the aperture of the cavity.

Both the realizable k- ϵ with enhanced wall treatment and the SST k- ω turbulence model is used for the CFD simulations, with the same inlet turbulence intensity specified as that listed in Scholten & Murray (1998b). It can be seen that although some of the distribution trends are captured, e.g., the pressure recovery in the wake, especially by the SST k- ω model, the detail distributions are inaccurate due to the inability of the fully-turbulent Reynolds-Averaged Navier-Stokes (RANS) approach to model the laminar-to-turbulent transition of the boundary layer before separation. This means that the peak Nusselt number at the stagnation point ($\theta = 0^\circ$) is under-predicted by between 15 and 20%, with the prediction accuracy increasing with Reynolds number. The average Nusselt numbers do however compare favourably (between 1 and 10%) with the experimental data. From this latter fact, it can be deduced that the average external forced convection heat transfer can be predicted fairly well using the RANS approach.

As a summary of the numerical validation, the following conclusions can be made:

- Although the RANS turbulence models are not able to accurately predict the detail heat transfer distribution due to the laminar-turbulent transition around a tube in cross-flow,

they give a fairly accurate prediction of the average convection heat transfer.

- As the mesh around the tube is refined, the predicted pressure distribution becomes more accurate for a tube within a tube bank. This prediction implies that the pressure drop over a tube bank can be predicted to an acceptable degree of accuracy in order to observe trends for optimization purposes.
- The realizable $k-\epsilon$ turbulence model is better at predicting the pressure distribution for coarser meshes, but is comparable with the SST $k-\omega$ turbulence model at predicting convection heat transfer for coarser meshes (not shown). As mesh density is increased however, the SST $k-\omega$ model has increased accuracy in predicting the heat transfer in the tube wake, especially as the Reynolds number is increased to values that cause an early transition to a turbulent boundary layer.

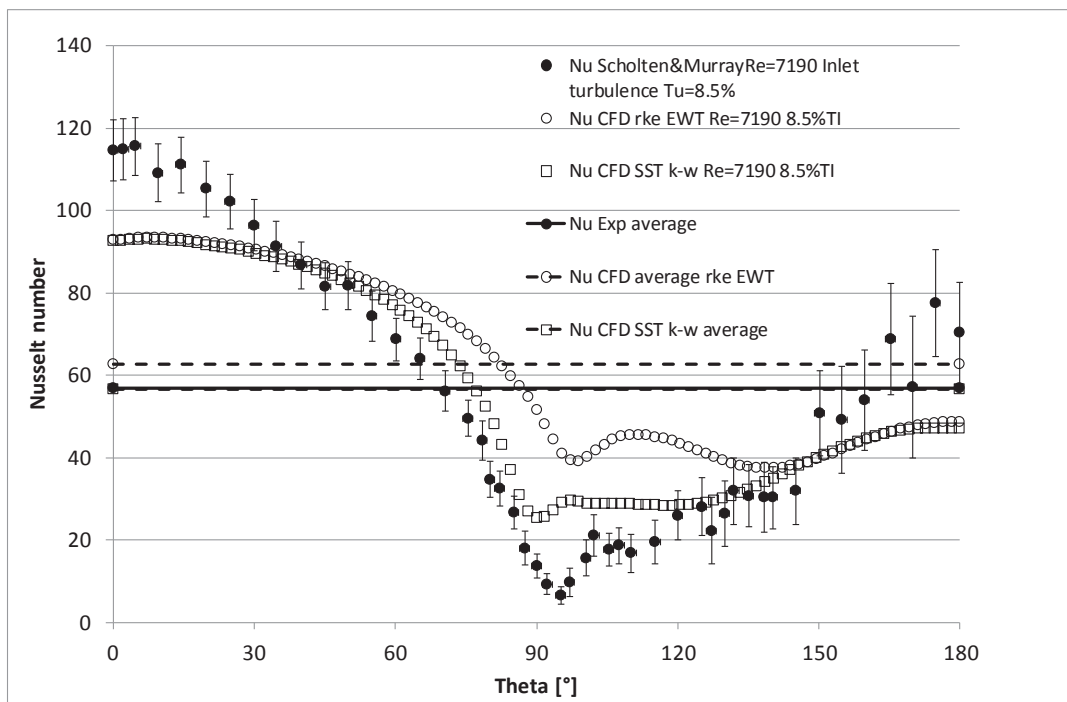


Fig. 17. Nusselt number distribution around cylinder: high inlet turbulence experiment versus realizable $k-\epsilon$ turbulence model for $Re = 7190$.

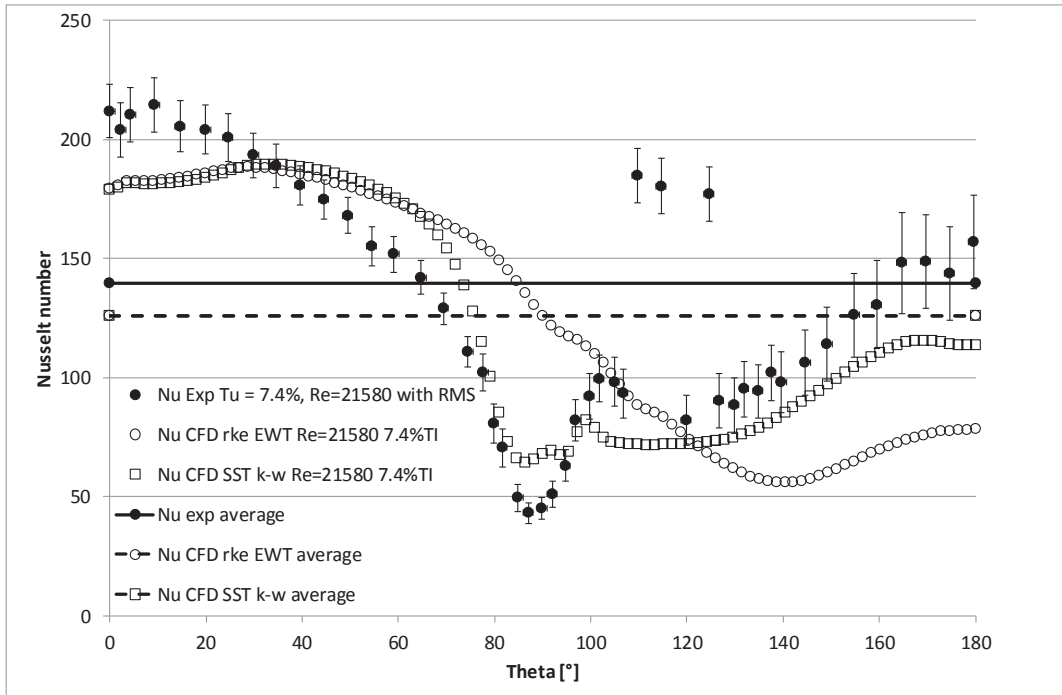


Fig. 18. Nusselt number distribution around cylinder: high inlet turbulence experiment versus realizable $k-\epsilon$ turbulence model for $Re = 21580$.

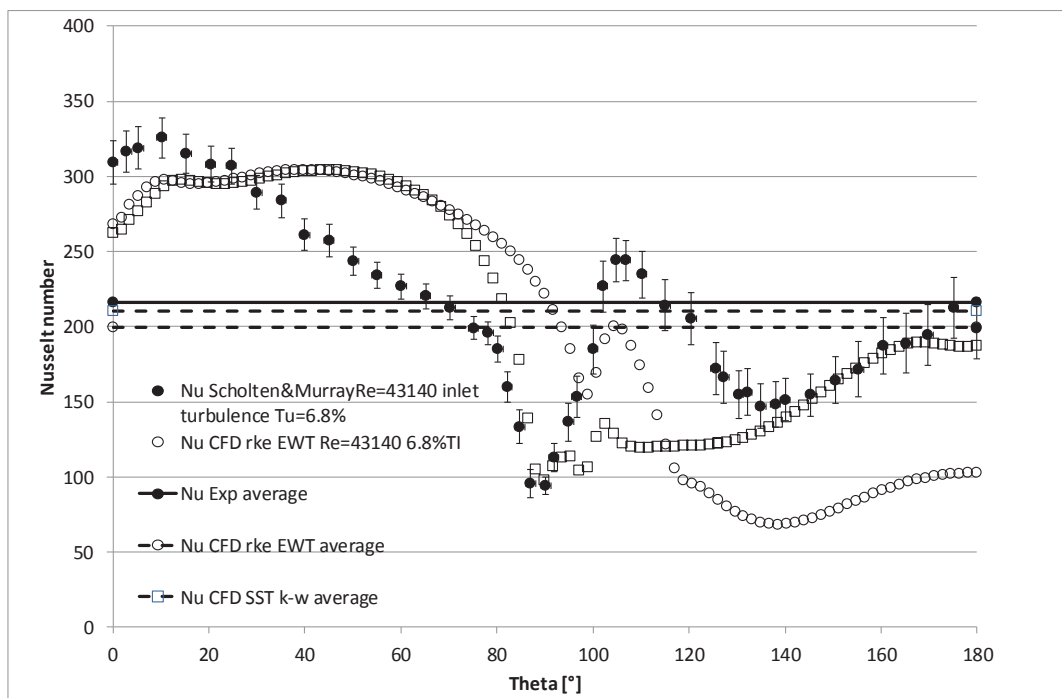


Fig. 19. Nusselt number distribution around cylinder: high inlet turbulence experiment versus realizable $k-\epsilon$ turbulence model for $Re = 43140$.

5.2. Solar irradiation

The solar irradiation is modeled in a similar fashion as for the test case in Section 2. The result of the radiation flux entering the cavity for the single gray band is shown in Fig. 20 together with the radiation flux absorbed by the tubes and that reflected by the cavity walls. Emission is again limited by setting all the cavity surface temperatures to 10K to isolate the solar heat load as an illustration. The resultant integrated flux on the cavity aperture was 1.035MW/m^2 or just over a 1000 suns for the source values used. The solar component of absorbed flux on the tubes is also plotted in Fig. 25a) as a function of position into the cavity. It can clearly be seen how the absorbed flux decays into the cavity because of the blocking effect of the tubes. Fig. 25a) also includes the combination of the solar and re-radiated component as discussed in Section 5.5.

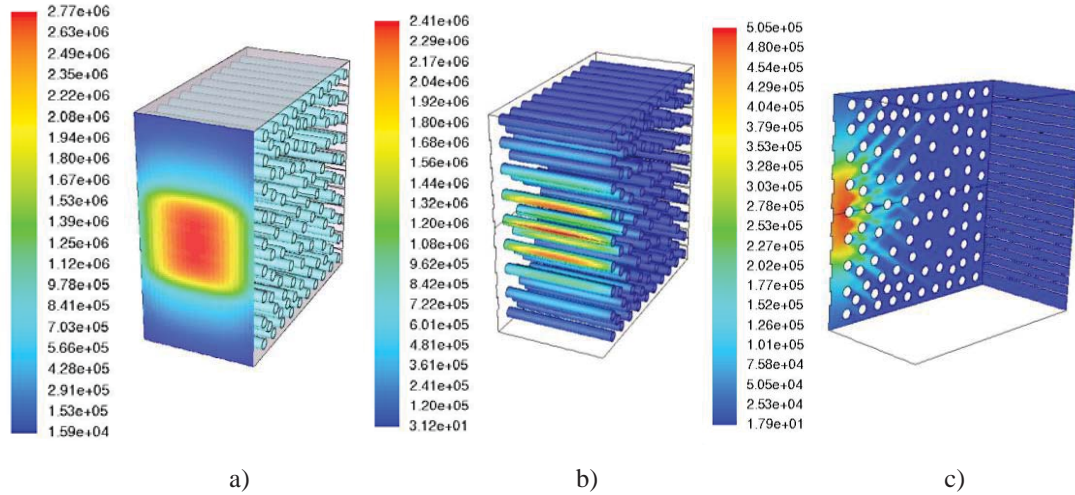


Fig. 20. a) Radiation flux at cavity aperture, b) Solar irradiation absorbed by tubes, c) Radiation reflected by cavity walls. All $[\text{W/m}^2]$. Single gray band.

To assess the influence of the assumed idealized solar heat flux map, a more realistic solar irradiation heat flux map was generated using SolTrace for the PS10 heliostat field in Seville, Spain (Marsberg et al, 2014). The heat source was scaled to be comparable to the heat flux depicted in Fig. 4a). The resulting source distribution at the semi-transparent wall location aimed at the cavity is shown in Fig. 21. When applying this heat source to the HPAR cavity the tube absorbed radiation and wall reflected radiation flux contours are as shown in Fig. 22a) and b), respectively. These should be compared to Fig. 20b) and c), respectively. It can be seen that the more diffuse source distribution due to the individual heliostats causes patterns of tube absorbed radiation (Fig. 22a))

and cavity wall reflected radiation (Fig. 23b)) that are also more diffuse. The integrated effect of this more realistic solar source is discussed in section 5.6.

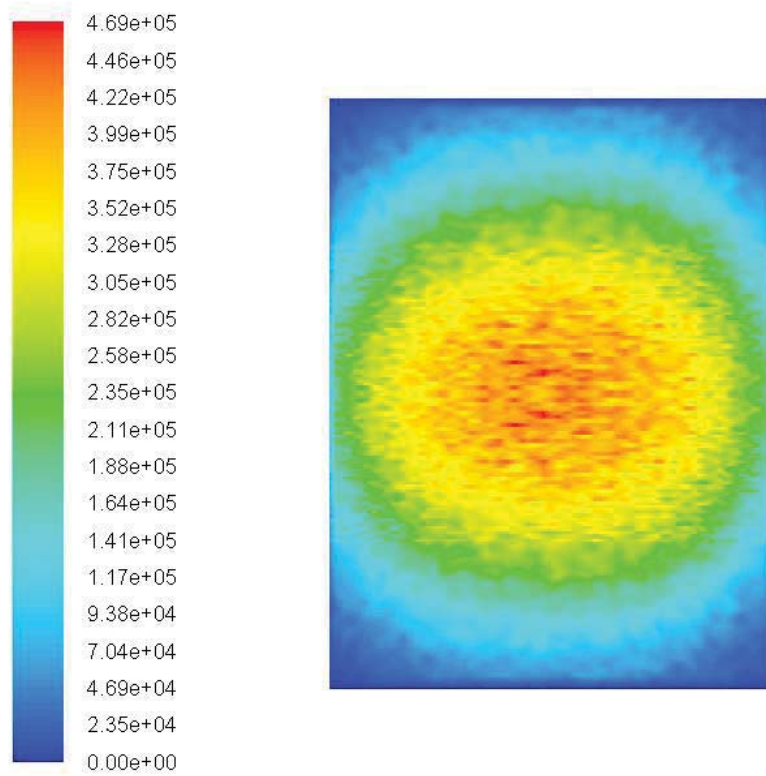


Fig.21. Effective source flux distribution [W/m^2] at inlet of computational domain based on PS10 heliostat field layout.

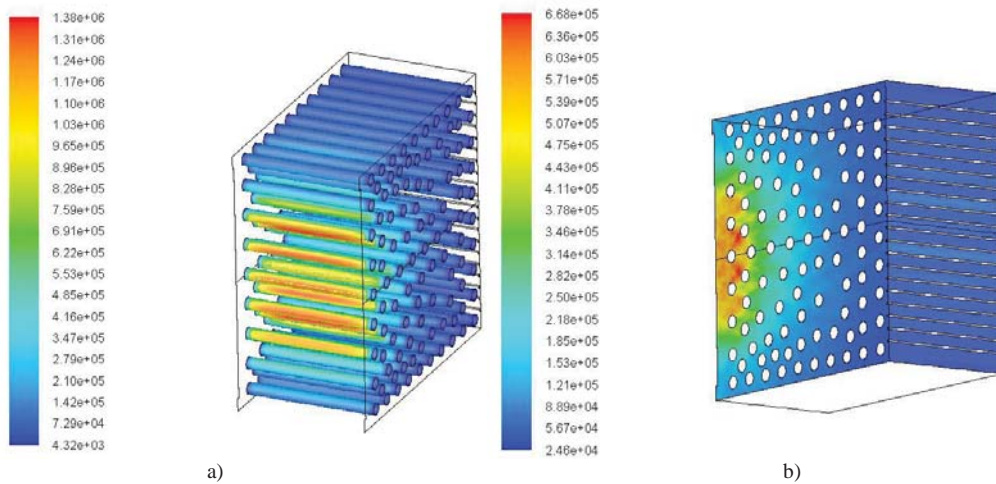


Fig.22. a) Solar irradiation absorbed at tubes for PS10 source; b) Radiation reflected by cavity walls for PS10 source. All [W/m^2].

5.3. Effect of porosity on forced convection flow patterns

A 2-D case was simulated to illustrate the effect of tube arrangement on the expected forced convection flow patterns and hence convective heat transfer in the cavity. A regular triangular arrangement, as would typically be found in a conventional heat exchanger was compared to a variable porosity layout with fewer tubes. Larger spacing between tubes would allow deeper penetration of solar irradiation, but should also allow more cooling fluid to pass through because of the lower flow resistance. It can be seen in Fig. 23 that short-circuiting of the cooling fluid between tubes is possible depending on the exact location of the inlet slots. The aim would be to optimize this flow distribution to investigate whether this would result in improved heat transfer at lower tube temperatures (see sample displayed in Fig. 23c)).

5.4. Heating of HTF

To illustrate the flow and temperature patterns inside the HTF loop, and how even the distribution of flow from the headers is into a vertical bank of tubes, Fig. 24 shows the flow patterns and temperature distribution for a 0.15kg/s mass flow rate at 1MPa pressure with the solar heating applied as illustrated in Fig. 20. The heating of the HTF is relatively even per pass through the cavity with the exception of the first row where the highest solar flux is experienced. This phenomenon suggests use of either different coatings on this set of tubes, or using solid quartz tubes as a buffer for this first row. Note the use of splitter plates in the headers to prevent short-circuiting of the header pipes into a specific set of tubes (located close to the header pipe outlet) in a vertical bank.

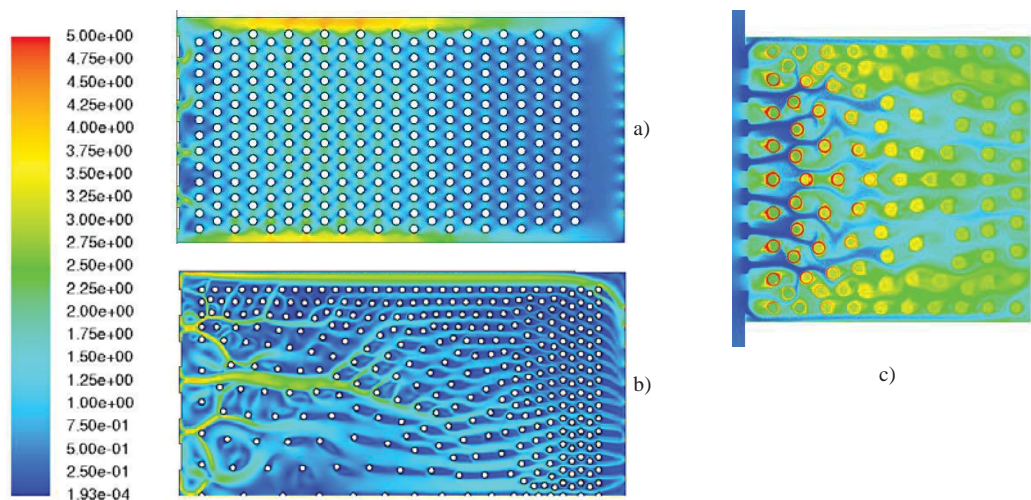


Fig. 23. Velocity magnitude contours for cavity forced convection flow a) regular triangular arrangement, b) symmetric half of elliptical porous region [m/s], c) Sample temperature contours in cavity for case displayed in Fig.8b).

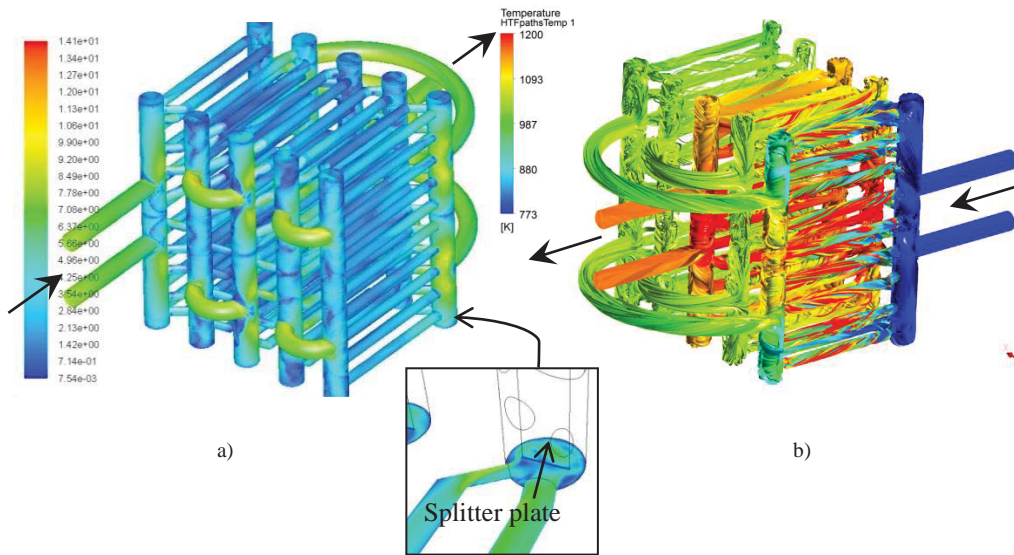


Fig. 24. HTF flow in tubes and headers a) Velocity magnitude contours [m/s], b) Pathlines colored by Temperature [K], clipped at 1200K. Single gray band.

5.5. Absorption of radiation and re-radiation

When the conjugate heat transfer problem is solved, the tubes and cavity walls heat up due to the incoming solar irradiation and then also emit radiation that is proportional to the emissivity and the fourth power of temperature. The effect of this additional heat transfer mechanism can be seen in the sample plot of absorbed radiation flux on the cavity tubes versus position into the cavity in Fig. 25a). It can be seen that the re-radiation effect causes the absorbed radiation profile to penetrate deeper into the cavity when comparing the solar-only (corresponding to the plots in Fig. 20) distribution with the combined solution. Fig. 25 also shows a sample tube outside temperature (Fig. 25b)) and the heat flux transferred to the HTF on the internal tube surface (Fig. 25c)). The tube temperatures are unrealistically high, indicating that there is room for improvement in an optimization process. The glass cover data are also shown on this plot and will be discussed in Section 6. Fig. 25d) and 25e) show the Nusselt number distributions on the tubes throughout the cavity, calculated according to equation (4) for the case without and with a glass window. The negative values correspond to sections of the tube where the heat transfer is negative, i.e., heat is given off by the tubes due to the cooling effect towards the rear of the cavity. The effect of the glass window is to increase the heat transfer for the similar temperature values, thereby increasing the Nusselt number. Note that the Nusselt number ranges are similar to those obtained in the numerical

validation study (Figs. 15 through 19), especially for the tubes at the front of the cavity.

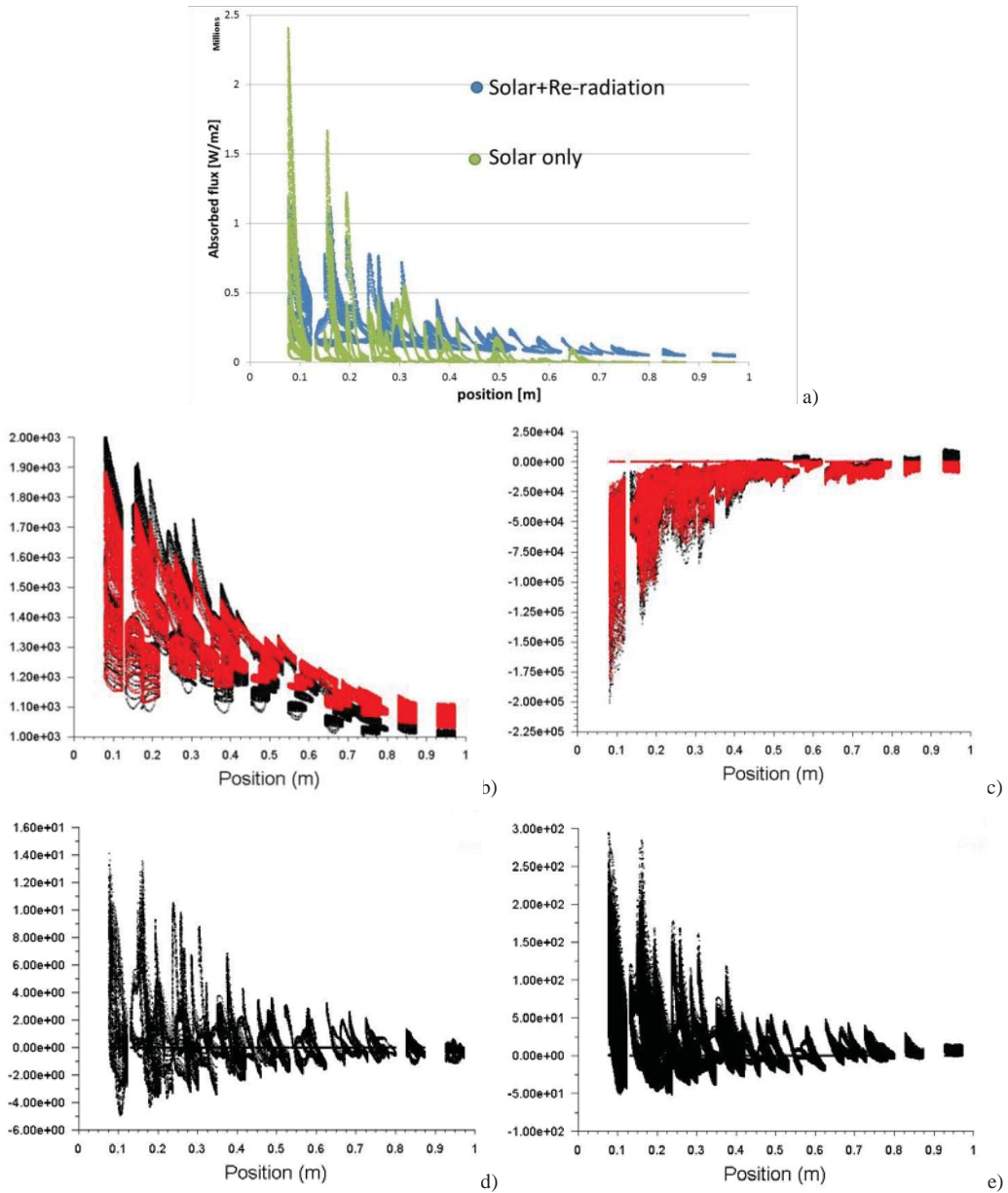


Fig. 25. As a function of position into cavity: a) Absorbed radiation flux on tubes (solar only versus solar and re-radiated) [W/m²] (Single gray band); b) Tube outside surface temperature [K] (Black – without glass; Red – with glass cover); and c) Tube internal transferred heat flux [W/m²] (Black – without glass; Red – with glass cover); d) Nusselt number on tube outside surface (without glass); e) Nusselt number on tube outside surface (with glass).

5.6. Influence of solar source distribution

Using the more realistic PS10 heat source (Fig. 21) in the simulation of the HPAR cavity, results in a slight change in the temperature distribution (Fig. 26a)) of the tubes located towards the front of the cavity. The tube internal heat transfer (Fig. 26b)) remains largely unchanged. It therefore seems as if the source distribution does not play a large role in the overall cavity performance. This statement needs to be verified for more realistic ray directions and resolution in the discrete ordinates model. In this comparison, the rays were all focused at the cavity center as for the ideal source.

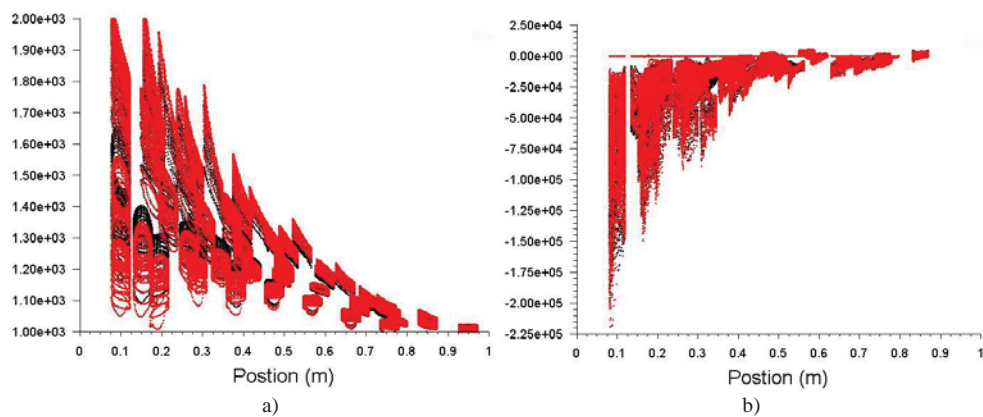


Fig. 26. As a function of position into cavity: a) Tube outside surface temperature [K] (Black – ideal source; Red – PS10 solar source); and b) Tube internal transferred heat flux [W/m²] (Black – ideal source; Red – PS10 solar source). Both without glass window, SST k- ω turbulence model.

6. Effect of glass window

6.1. Influence of glass on heat transfer

To illustrate the greenhouse effect of the glass window cover, the cavity tube surface temperatures are compared side-by-side in Fig. 27. The main effect of the glass is to reduce the maximum temperature but also to increase the minimum tube outside temperature. The exact values are tabulated in Tab. 2 together with the cavity and HTF outlet temperatures. The net effect of the glass cover on the HTF is to increase the outlet temperature leading to a 9% increase in the heat transferred to the HTF. Fig. 27 shows that for the glass cover case, the tubes behind the first row are hotter because of the reflected re-radiation off the glass internal surface. This means that more heat can be transferred to the HTF in this region. The phenomenon is confirmed in Fig. 25b),c) where the effect of the glass cover on the spatial distribution of tube outside temperature and tube inside surface heat transfer is displayed. The main gain in heat transferred is in the last few rows of tubes in the cavity. Without a glass cover, these tubes actually had a *negative* absorption of heat.

The increase in cavity outlet air temperature with a glass cover needs to be investigated. This warmer air can be used to preheat the HTF and/or it can be used to heat a packed-bed storage container in conjunction with the air from the turbine downstream of the cavity. The mass flow rate of the ambient-pressure cavity air is low compared to the assumed compressor flow rate (8.3%), so the influence of the exact value needs to be investigated. Increasing the cavity flow rate would be beneficial for lowering tube temperatures but would require extra power that would decrease the efficiency of the HPAR system.

Case	HTF inlet temperature [K]	HTF outlet temperature [K]	Cavity outlet temperature [K]	Minimum tube temperature [K]	Maximum tube temperature [K]
No glass cover (SST k- ω model)	773	1162	742.7	993	2001
With glass cover (base mesh, SST k- ω model)	773	1196	1026	1026	1887
With glass cover (base mesh, realizable k- ϵ model)	773	1204.6	1108.6	1053	1883
With glass cover (Adapt 1, realizable k- ϵ model)	773	1205.3	1108.4	1052	1884

With glass cover (Adapt 2, realizable k-ε model)	773	1205.4	1107.4	1040	1884
--	-----	--------	--------	------	------

6.2. Influence of mesh around tubes

To illustrate the mesh dependency of the glass solution, Table 1 also includes the integrated results for the case with a glass window with increasing levels of mesh adaption on the tube outer walls. These simulations were performed with the realizable k-ε turbulence model with enhanced wall treatment and therefore also provide a comparison of turbulence models for the base mesh. The change in turbulence model did not significantly affect the HTF outlet or maximum tube temperature, but made a 7% difference in the cavity outlet temperature and resulted in a 3% change in the tube minimum temperature. A close-up of the three meshes of the region close to the outlet slots is shown in Fig. 28.

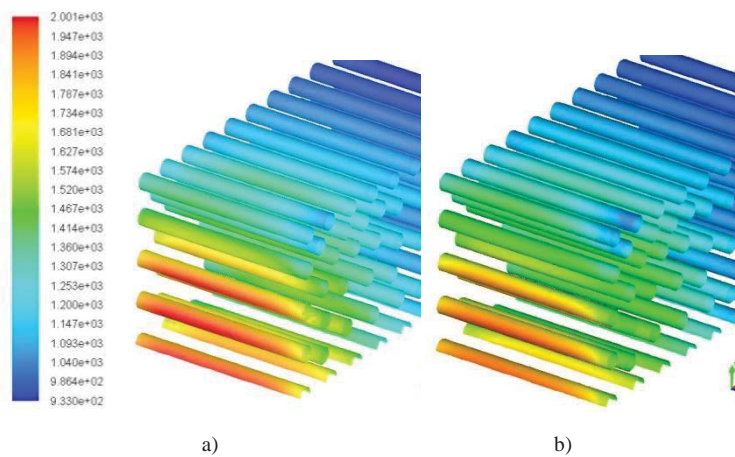


Fig. 27. Cavity tube surface temperature a) No glass cover b) With glass cover.

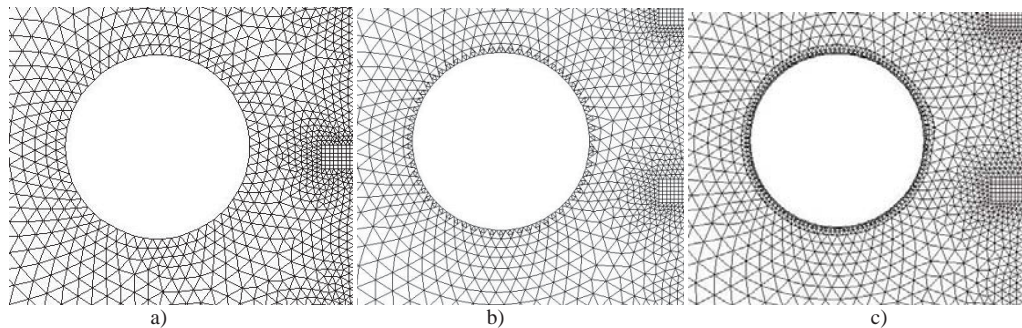


Fig. 28. Mesh around tubes in HPAR cavity a) Original b) Adapted once c) Adapted twice.

6.3. Influence of turbulence model

Based on the numerical validation study, it was shown that the realizable $k-\varepsilon$ and SST $k-\omega$ turbulence models each have their own advantages. For the case with a glass cover, the resulting tube outside diameter temperature and tube inside diameter heat transfer distributions as a function of cavity position in Fig. 29 are seen to be only slightly affected by the choice of turbulence model.

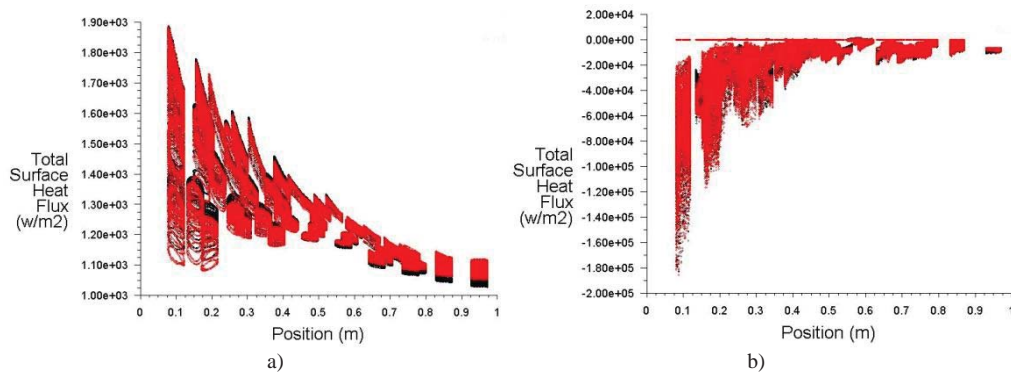


Fig. 29. As a function of position into cavity (no glass window): a) Tube outside surface temperature [K] (Black – SST $k-\omega$ turbulence model; Red – realizable $k-\varepsilon$ turbulence model); and b) Tube internal transferred heat flux [W/m^2] (Black – SST $k-\omega$ turbulence model; Red – realizable $k-\varepsilon$ turbulence model).

7. Candidate performance parameters

The obvious choice for objective function in an optimization formulation is a measure that maximizes heat transfer between the incoming solar irradiation and the heat transfer fluid (HTF). In order to maximize this heat transfer the losses must be minimized. As the aim of the HPAR is to mimic a volumetric receiver using multiple tubes, the profile of heating is also important (Fend, 2012, Kretschmar & Gauché, 2012). The shape of the temperature distribution and absorbed radiation distribution into the cavity can also be measures that can be included in an optimization problem formulation. Other candidates include:

- Deviation from an even temperature profile on the tube faces
- Temperature gradient(s) and associated differential thermal expansion on structural components
- Irreversibility, entropy generation (2nd law efficiency)
- Exergy destruction in specific regions of the cavity

- Heat transfer mechanism budget in different zones (radiative vs convective vs conductive)
- Cooling power required for tube external forced convection (flow rate \times pressure drop obtained from CFD simulation)

8. Conclusions and recommendations

The paper has described the analysis of a hybrid pressurized air cavity receiver using CFD. The following conclusions can be made:

- CFD is able to model solar irradiation targeted at a cavity receiver in combination with the conjugate heat transfer problem. The Discrete Ordinates radiation model allows for both solar irradiation and re-radiation to be solved simultaneously.
- A cavity receiver geometry can be parameterized so that parameters can be assigned as design variables in a subsequent optimization problem solution. The scripting capability of GAMBIT can be used to generate the geometry and mesh in a fairly automated fashion.
- A semi-gray radiation model can be implemented to model the selective absorption of a glass cover for the cavity as well as allowing for spectral-selective emittance and hence absorptance properties of cavity surfaces, including tubes conveying the HTF.
- In a comparison of the effect of re-radiation on the thermal efficiency due to the presence of a glass cover, a 9% increase in heat transferred to the HTF was obtained for the operating conditions used. With the glass cover modeled, the range of tube temperatures as well as the maximum tube temperature was reduced, both being desirable features.
- Different performance parameters can be extracted from the CFD solution that can serve as objective functions and constraints in an optimization problem definition.

Future work includes the optimization of the cavity receiver for a set of conditions. These include extension of the heliostat source definition, different operating conditions of the HPAR, and an extension to include a secondary heat exchanger. More representative optical properties, i.e., solar absorptance, reflectance, transmittance and thermal emissivity as a function of at least wavelength and temperature (using a hemispherical assumption to eliminate variation due to the two solid angles) will be considered for coatings on the cavity tubes and walls. These can be implemented using User-Defined Functions (UDFs) in ANSYS Fluent.

Acknowledgements

The authors would like to acknowledge the support from the University of Pretoria (South Africa) and the South African National Research Foundation (DST-NRF Solar Spoke).

References

- Allen, K.G., von Backström, T.W., Kröger, D.G., 2013. Packed rock bed thermal storage in power plants: Design considerations. SolarPaces 2013, 17-20 September, Las Vegas, Nevada, USA.
- ANSYS, 2012. Fluent 14.5 User's Guide.
- Ávila-Marín, A.L., 2011. Volumetric receivers in Solar Thermal Power Plants with Central Receiver System technology: A review. *Solar Energy*, 85:891–910.
- Craig KJ, Gauché P, Kretzschmar H., 2013. Optimization of solar tower hybrid pressurized air receiver using CFD and mathematical optimization. SolarPaces 2013, 17-20 September, Las Vegas, Nevada, USA.
- Ercoftac classic database, 2014. <http://cfd.mace.manchester.ac.uk/ercoftac/>, accessed 1 August 2014.
- Fend T., 2010. High porosity materials as volumetric receivers for solar energetics. *Optica Applicata*. XL No. 2:271-284.
- Hachicha, A.A., 2013. Numerical modelling of a parabolic trough solar collector, PhD thesis, Polytechnic University of Catalunya, Terrassa.
- Hoffschmidt, B., Téllez, F.M., Valverde, A., Fernández, J., Fernández, V. 2003. Performance Evaluation of the 200-kWth HiTRec-II Open Volumetric Air Receiver. *ASME Journal of Solar Energy Engineering*. 125:87-94.
- Kretzschmar H., 2014. The Hybrid Pressurized Air Receiver (HPAR) for combined cycle solar thermal power plants. M.Sc.Eng. thesis, Stellenbosch University, South Africa.
- Kretzschmar H., Gauché P., 2012. Hybrid pressurized air receiver for the Sunspot cycle. 1st South African Solar Energy Conference (SASEC), 21-23 May 2012.
- Marsberg, J., Craig, K.J., Meyer, J.P., 2014. Heliostat field heat flux map generation for CFD optimization of central receiver. SolarPaces 2014, 16-19 September, Beijing, China.
- Mahon, J., Meskell, C., 2009. Surface pressure distribution survey in normal triangular tube arrays. *J. Fluids Structures*, 25:1348-1368.
- Modest, M.F., 2013. *Radiative Heat Transfer*, third ed. Elsevier.
- Sano Y, Iwase S, Nakayama A., 2012. A local thermal nonequilibrium analysis of silicon carbide ceramic foam as a solar volumetric receiver. *J Solar Energy Engineering*. 134:021006-1:021006-8.

Scholten, J.W., Murray, D.B., 1998a. Unsteady heat transfer and velocity of a cylinder in cross flow- I. Low freestream turbulence, *Int. J. Heat Mass Transfer*. 41(10):1139-1148.

Scholten, J.W., Murray, D.B., 1998b. Unsteady heat transfer and velocity of a cylinder in cross flow -II. High freestream turbulence. *Int. J. Heat Mass Transfer*. 41(10):1149-1156.

Smirnova O, Fend T, Schwarzbözl P, Schöllgen D, Höhe L., 2010. Homogeneous and inhomogeneous model for flow and heat transfer in porous materials as high temperature solar air receivers. *Proceedings of the COMSOL Conference 2010 Paris*.